

# Nexus: Efficient and Scalable Multi-Cell mmWave Baseband Processing with Heterogeneous Compute

Zhenzhou Qi, Chung-Hsuan Tung, Zhihui Gao, Tingjun Chen

Department of Electrical and Computer Engineering, Duke University

## Abstract

The rapid adoption of 5G New Radio (NR), particularly in the millimeter-wave (mmWave) spectrum, imposes stringent demands on the flexibility, scalability, and efficiency of baseband processing. While virtualized Radio Access Networks (vRANs) enable dynamic spectrum sharing across cells, compute resource allocation for baseband processing, especially in multi-cell deployments with heterogeneous workloads, remains underexplored. In this paper, we present Nexus, the first system to realize real-time, virtualized multi-cell mmWave baseband processing on a single server with heterogeneous compute resources. Nexus integrates software-based digital signal processing pipelines with hardware-accelerated LDPC decoding, and introduces a novel framework for sharing Intel’s ACC100 eASIC across multiple CPU cores via virtual functions (VFs). For single-cell operation, Nexus employs a random forest (RAF)-based model that predicts the most energy-efficient resource allocation for the given cell configuration with microsecond-level inference latency and high accuracy. For multi-cell scenarios, Nexus introduces a power-aware scheduler that incorporates a lightweight contention model to adjust resource allocation strategies under concurrent execution. Through extensive evaluation across various Frequency Range 2 (FR2) cell configurations, we show that Nexus supports up to 16 concurrent cells under full load, achieving 5.37 Gbps aggregate throughput, while reducing the multi-cell scheduling search space by orders of magnitude. These results demonstrate that virtualized, resource-aware baseband processing is both practical and efficient for next-generation vRAN systems.

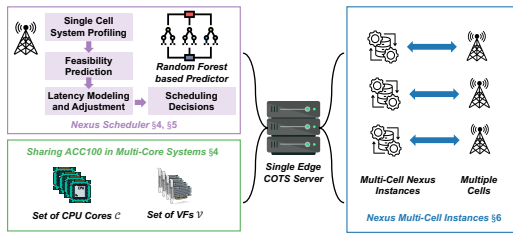
## 1 Introduction

5G New Radio (NR) has rapidly evolved to become the foundation for modern wireless communication systems, aiming to deliver ultra-high throughput, ultra-low latency, and massive device connectivity [3]. A key feature of 5G NR is its flexible subcarrier spacings and slot durations to adapt to a variety of deployment scenarios. Combined with large bandwidth support and operation across diverse frequency ranges, including the millimeter-wave (mmWave) spectrum in Frequency Range 2 (FR2) [6], 5G NR is pushing the limits of both radio access and infrastructure design [20, 28, 29].

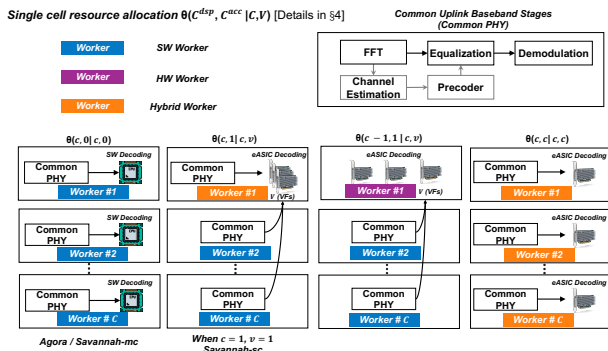
To meet growing performance demands, the wireless industry is transitioning from dedicated hardware toward centralized Radio Access Network (RAN) [10, 12, 42], and further into disaggregated, software-defined architectures such as virtualized RAN (vRAN) [14, 16, 27] and Open RAN (O-RAN) [36, 40]. These architectures decouple baseband functions from specialized hardware, allowing deployment on general-purpose compute platforms with heterogeneous compute resources, including CPU, GPU, FPGA, and ASICs. This shift reduces capital expenditure and enables key capabilities such as dynamic network slicing, centralized scheduling, coordinated beamforming, and elastic scaling of compute resources across diverse baseband workloads.

While significant research and development have focused on the virtualization of radio resources, e.g., dynamic Physical Resource Block (PRB) sharing [8], little attention has been given to sharing computational resources in vRAN. These computational resources, such as CPU cores, hardware accelerators (e.g., ASICs), and memory bandwidth, are just as critical as radio spectrum in determining the system’s capacity, performance, and responsiveness. As 5G moves toward dense, high-throughput deployments, the ability to efficiently share and schedule computational resources across cells becomes essential.

In this paper, we present Nexus, the first system that enables efficient, virtualized multi-cell mmWave baseband processing on a single server with heterogeneous compute resources, including CPUs and ASICs. Nexus addresses the key challenge of scaling computational resources across multiple FR2 cells while guaranteeing the strict real-time processing deadlines imposed by 5G NR. Designing Nexus introduces several technical challenges. First, uplink Physical layer (PHY) processing in FR2 with numerology 3 and channel bandwidths up to 400 MHz imposes extreme computational demand, especially under full traffic load. Second, integrating hardware accelerators such as Intel’s ACC100 eASIC for LDPC decoding into a shared multi-core vRAN environment requires careful coordination between CPU-based digital signal processing (DSP) stages and accelerator offloading, where queueing and PCIe transfer overheads can create unpredictable bottlenecks. Third, efficiently supporting heterogeneous cells requires a resource allocation framework



(a) Nexus Overview



(b) Resource Allocation Strategies

**Figure 1: Overview of Nexus: (a) Nexus virtualizes multi-cell mmWave PHY processing on a single server with heterogeneous compute by sharing a set of CPU cores and a pool of ACC100 virtual functions (VFs) in a power-aware manner. (b) Resource allocation strategies for a single cell are characterized by combinations of CPU cores and VFs.**

that can (i) adapt allocations to diverse PHY layer parameters, and (ii) account for latency contention effects when multiple cells run concurrently on the same server.

To overcome these challenges, Nexus introduces a complete system architecture (Fig. 1). It features the first detailed design for sharing ACC100 accelerators across multiple worker cores via virtual functions; a random forest (RAF)-based model that maps PHY-layer features, or *cell configurations*, to the most energy-efficient resources required for each cell; and a power-aware scheduler for both single-cell and multi-cell scenarios, the latter integrating a lightweight contention model to ensure per-cell latency guarantees under concurrent execution. We extensively evaluate Nexus across various deployment scenarios. At the model level, we characterize the performance of our RAF-based predictor in detail. We compare it against six baselines, including three deep learning (DL) models and three analytical approaches, showing that RAF achieves near-DL accuracy with two orders of magnitude faster inference, smaller latency variance, and modest model size. We further demonstrate that the RAF model generalizes well to unseen single-cell configurations, sustaining  $> 98\%$  prediction accuracy. At the system level, we validate Nexus under diverse deployment scenarios. We show that Nexus supports up to sixteen concurrent cells with

a total data rate of 5.37 Gbps using sixteen CPU cores and sixteen ACC100 VFs, with the ability to scale further.

In summary, this paper makes the following contributions:

- We present Nexus, the first system supporting real-time, virtualized multi-cell mmWave baseband processing on a single server with heterogeneous compute resources (CPUs and ASICs). This includes the first ACC100 sharing framework across multiple cores, enabling flexible offloading modes and scalable LDPC decoding;
- We design an RAF-based model that maps cell configurations to the most energy-efficient resource allocation required to meet the PHY processing deadline. For multi-cell deployments, we develop a contention-aware extension of the RAF scheduler that captures system-level compute resource contention across cells;
- We extensively evaluate Nexus on a heterogeneous compute testbed, demonstrating robust support for up to 16 concurrent FR2 cells at 100% traffic load, achieving over 5.37 Gbps aggregate throughput while meeting the 3-slot PHY processing deadline.

The codebase and measurements of Nexus are open-sourced [2].

## 2 Related Work

**mmWave testbeds** mmWave communication has emerged as a key enabler for high-throughput wireless systems, with its expansive spectrum in the 24–52 GHz range accommodating higher data rates than sub-6 GHz technologies. The unique propagation characteristics in mmWave bands, such as higher path loss and susceptibility to blockage, have spurred research into advanced beamforming and beam management techniques that counteract short coverage ranges and ensure robust connectivity [15, 41]. To evaluate these strategies in realistic settings, a number of testbed [26, 30] have been proposed, including, programmable phased-array antennas [32], and prototype 5G NR FR2 equipment [46].

**PHY Baseband Processing and Virtualization** Traditional baseband processing relies on specialized hardware accelerators or Digital Signal Processors (DSPs) capable of handling computationally intensive tasks. The advancement of virtualization techniques and cloud-native paradigms such as Sora [38], BigStation [45], Agora [11], Hydra [19] and Savannah [27] have driven a shift toward software-implemented PHY stacks on commodity hardware, often hosted on general-purpose CPUs, GPUs, or specialized accelerators. This virtualization of baseband functions allows network operators to allocate and scale resources based on changing load conditions, while also enabling easier deployment of updates and new features. To the best of our knowledge, our work is the first to specifically target virtualized multi-cell baseband

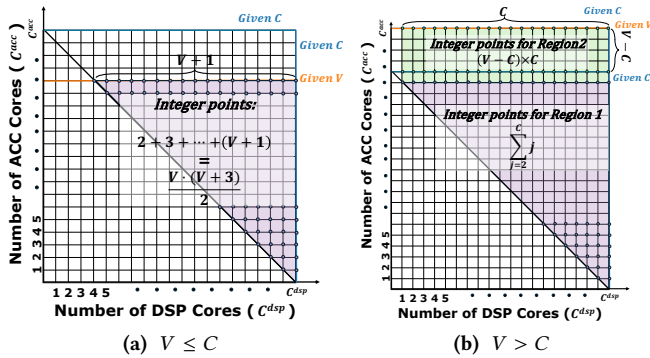


Figure 2: Region of resource allocations, where integer points in the shaded area represent valid CPU core and VF allocations satisfying (1)–(2).

processing in a single server, pushing beyond the typical single-cell or multi-server setups explored in prior literature.

**Heterogeneous Computing and Resource Sharing** Recent interest in heterogeneous computing has spurred work on efficiently utilizing diverse processing elements [33, 39], such as CPUs, GPUs, and FPGAs, to tackle the demanding computational requirements of next-generation wireless networks. While many studies have extensively explored radio resource sharing, for example, dynamic allocation of physical resource blocks (PRBs) among different users [8], relatively few have focused on computational resource sharing, especially in environments where multiple heterogeneous processors coexist within the same physical infrastructure. This gap highlights a pressing need for strategies that can effectively partition, schedule, and manage such resources without compromising performance or scalability in high-frequency, high-bandwidth scenarios.

### 3 Preliminaries

**5G NR frame structure and numerology.** The 5G NR frame structure supports multiple numerologies for operation across a wide range of carrier frequencies, including the mmWave bands in FR2. FR2 spans 24.25 GHz–52.6 GHz and commonly utilizes numerology 3 ( $\mu = 3$ ), which corresponds to a subcarrier spacing (SCS) of 120 kHz. This work therefore focuses on  $\mu = 3$ . Compared to the standard 15 kHz subcarrier spacing used in Frequency Range 1 (FR1, sub-6 GHz), the higher SCS of 120 kHz reduces OFDM symbol duration, making it more suitable for high Doppler spreads and low-latency requirements. At  $\mu = 3$ , each slot spans 0.125 ms with 14 symbols,  $8\times$  shorter than the 1 ms slot at 15 kHz [5].

**Baseband Processing.** Baseband processing refers to the digital signal processing tasks required to encode and decode user data for wireless transmission. Fig. 1(b) shows uplink operations such as FFT, channel estimation, equalization, demodulation, and forward error correction (FEC) before

Table 1: Parameters of considered cell complexity, denoted by  $\sigma(M, B, \rho_t, \rho_f, \chi)$  and based on [4].

Dimension	Notation	Range	Granularity
Channel BW	$B$	{100, 200, 400} MHz	Discrete
MIMO Size	$M$	{1, 2, 4}	Discrete
Traffic Load	$\rho_t$	[0,100] %	6.25%
Transmission BW %	$\rho_f$	[0,100] %	Multiple PRBs
MCS Index	$\chi$	{0, 1, ..., 28}	Integer

the MAC layer. These tasks are performed after the radio unit (RU) captures the user’s signal and streams the raw I/Q samples to the processing unit. 5G NR functional split options [3] define how these tasks are partitioned across the radio access network (RAN). This work focuses on split option 8, where the entire baseband stack is centralized in the distributed unit (DU). This configuration enables flexible compute resource pooling across multiple cells, which is critical in supporting dynamic, multi-cell vRAN deployment. Notably, uplink baseband processing is significantly more computationally intensive than downlink due to the iterative nature of the brief propagation. As such, Nexus focuses exclusively on uplink processing. Prior studies such as FlexRAN [21] and Atlas [43] report that downlink symbol processing latency is typically  $\sim 3\times$  lower than uplink. Thus, demonstrating support for 100% uplink traffic load in Nexus implicitly ensures that the system can also sustain intensive downlink workloads under the 5G slot format.

### 4 Nexus for a Single Cell

Even though Nexus is designed to virtualize baseband processing across multiple mmWave cells, the effectiveness of multi-cell scheduling fundamentally depends on accurately understanding how compute resource allocation impacts baseband processing latency for a single cell against varying cell configurations. Our single-cell profiling and analysis reveal how CPU cores and ACC100 VFs interact, how power and latency trade off across resource allocations, and how cell configuration parameters shape computational demand.

However, two challenges make single-cell scheduling non-trivial. First, the possible resource allocation space is large: one cell can map to many combinations of CPU cores and ACC100 VFs, each with different power–latency characteristics. Second, feasibility, defined as whether the 99.9<sup>th</sup> percentile processing latency under a given allocation meets the strict 3-slot deadline, is not deterministic but varies nonlinearly with different cell configurations. To address these challenges, we first model the single-cell allocation space and quantify its brute-force complexity. We then introduce a random forest (RAF)-based feasibility model that efficiently predicts whether a given allocation can meet real-time processing deadlines, while significantly pruning the search

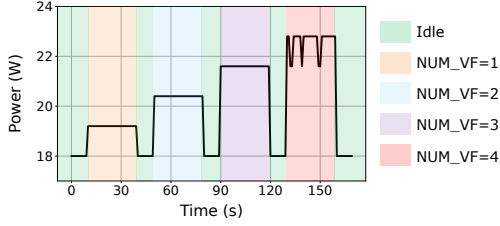


Figure 3: Power consumption of ACC100 with multiple VFs.

space. This single-cell framework enables Nexus to select energy-efficient resource allocations, and also serves as the building block for the multi-cell scheduler described in §5.

#### 4.1 Cell Configuration

Let  $\sigma(M, B, \rho_t, \rho_f, \chi)$  denote the *cell configuration*, which is a function of the cell's PHY parameters and workloads. Table 1 summarizes the range and granularity of these parameters based on the 3GPP Technical Specifications for FR2 [4]. Specifically, we consider the DDSU TDD frame structure, which allocates 52 downlink, 2 guard, and 16 uplink symbols across five slots, which is widely adopted in both industry and research [18, 22, 23], and is also recommended by 3GPP for its latency benefits [13]. Since we focus on uplink processing,  $\rho_t$  effectively has a granularity of  $1/16 = 6.25\%$ . The transmission BW percentage is defined relative to the maximum number of physical resource blocks (PRBs) supported for a given channel bandwidth. For example, with a 400 MHz channel at numerology  $\mu = 3$ , the maximum is 264 PRBs (see Table 5.3.2-1 in [7]). This corresponds to a granularity of  $1/264 \approx 0.38\%$ , where each PRB corresponds to 12 subcarriers, i.e.,  $12 \times 120 \text{ kHz} = 1.44 \text{ MHz}$ .

#### 4.2 Optimizing Heterogeneous Compute Resource Allocation

Consider a server equipped with  $C_{\max}$  CPU cores and supporting  $V_{\max}$  ACC100 accelerator virtual functions (VFs). We assume  $C_{\max} \geq V_{\max}$ , e.g., the server used in our experiments is with  $C_{\max} = 56$  and  $V_{\max} = 16$  using a single ACC100 accelerator card. To support a single cell using a set of CPU cores,  $C$ , and a set of ACC100 VFs,  $\mathcal{V}$ , we define the *single-cell resource allocation strategy* as  $\theta(C^{\text{dsp}}, C^{\text{acc}}|C, \mathcal{V})$ . Here,  $C^{\text{dsp}}$  and  $C^{\text{acc}}$  represent the sets of CPU cores allocated to software DSP and ACC100 offloading tasks, which are optimization variables given the available resources  $C$  and  $\mathcal{V}$ . Since all CPU cores are considered homogeneous and equivalent, the specific sets of cores assigned to different tasks are irrelevant; only the number of cores allocated to each task matters. Therefore, without loss of generality, this single-cell resource allocation can be represented by  $\theta(C^{\text{dsp}}, C^{\text{acc}}|C, V)$ , where  $C^{\text{dsp}} = |C^{\text{dsp}}|$ ,  $C^{\text{acc}} = |C^{\text{acc}}|$ ,  $C = |C|$ , and  $V = |\mathcal{V}|$ .

**Feasible resource allocation strategies.** For a given number of  $C \leq C_{\max}$  and  $V \leq V_{\max}$ , the heterogeneous compute resource allocation for a single cell needs to satisfy the following constraints describing the relationship between the DSP pipeline and utilized hardware resources:

- Each CPU core is dedicated to either software DSP, offloading LDPC decoding to ACC100, or both, i.e.,

$$1 \leq C = |C| = |C^{\text{dsp}} \cup C^{\text{acc}}| \leq C^{\text{dsp}} + C^{\text{acc}},$$

$$1 \leq C^{\text{dsp}} \leq C \text{ and } 1 \leq C^{\text{acc}} \leq C. \quad (1)$$

When ACC100 VFs are available, LDPC decoding is offloaded to the hardware accelerator, while the CPU cores are responsible for all remaining DSP tasks.

- Each CPU core responsible for ACC100 offloading tasks is mapped to a unique set of VFs, and each VF cannot be managed by more than one core, i.e.,

$$1 \leq C^{\text{acc}} \leq V. \quad (2)$$

For fixed values of  $C (\leq C_{\max})$  and  $V (\leq V_{\max})$ , let  $\Theta(C, V)$  denote the set of feasible allocations satisfying the above-mentioned constraints, i.e.,

$$\Theta(C, V) = \{\theta(C^{\text{dsp}}, C^{\text{acc}}|C, V) : (1)-(2) \text{ are satisfied}\}. \quad (3)$$

Fig. 2 illustrates this feasibility region (shaded areas), with each integer point  $(C^{\text{dsp}}, C^{\text{acc}})$  representing one feasible resource allocation strategy. It can be shown that the number of feasible allocations is:

$$|\Theta(C, V)| = \begin{cases} \sum_{j=1}^V (j+1) = \frac{V(V+3)}{2}, & \text{if } V \leq C, \\ \sum_{j=2}^C j + (V-C) \cdot C = \frac{2VC+C-C^2-2}{2}, & \text{if } V > C. \end{cases} \quad (4)$$

**Power-aware resource optimization.** Nexus addresses the challenge of efficiently selecting the allocation strategy to meet the stringent real-time PHY processing deadline in a virtualized baseband system, while minimizing the power consumption. This power-aware resource optimization is

$$\theta^* := \arg \min_{\theta} : P(\theta) = \alpha_1 P_1(C^{\text{dsp}}) + \alpha_2 P_2(C^{\text{acc}}) + \alpha_3 P_3(V) \quad (5)$$

$$\text{s.t.} : \mathcal{L}(\theta) < 3\text{-slot}, \theta \in \Theta(C, V) \text{ from (3),}$$

$$1 \leq C \leq C_{\max}, 1 \leq V \leq V_{\max}.$$

Here,  $P_1(C^{\text{dsp}})$ ,  $P_2(C^{\text{acc}})$ , and  $P_3(V)$  denote the power consumption of DSP worker cores, ACC100 offloading cores, and ACC100 VFs, respectively. The weights  $\{\alpha_1, \alpha_2, \alpha_3\}$  allow system designers to bias resource selection depending on hardware constraints, which are set to equal in Nexus, i.e.,  $\alpha_1 = \alpha_2 = \alpha_3 = 1$ . We use Intel's Performance Counter Monitor (PCM) [1] to measure the CPU power consumption. Each active core contributes approximately 7W of dynamic power, consistent with prior studies [27], yielding  $P_1(C^{\text{dsp}}) + P_2(C^{\text{acc}}) = 7 \cdot C$ . To characterize the power consumption of the ACC100, we conduct measurements on an

ACC100 connected to a workstation through a PCIe riser cable and isolate the 12 V supply for inline current measurement using a clamp meter following prior work [27, 31]. The measurement accuracy of this approach is validated using an NVIDIA GTX1070 GPU with the `nvidia-smi` tool. As shown in Fig. 3, each active ACC100 VF adds approximately 1.2 W power, yielding  $P_3(V) = 1.2 \cdot V$ .

### 4.3 Profiling and Exploring Resource Allocation Strategies

**Profiling methodology.** To understand how resource allocations  $\theta$  impact feasibility, we developed and instrumented the Nexus software stack to record per-frame processing latency across diverse cell configurations. Built on top of the Agora [11] and Savannah [27] codebases, Nexus extends support for multiple implementations, each corresponding to a distinct resource allocation strategy. This required substantial engineering effort to enable flexible switching between software-only, hardware-accelerated, and hybrid paths (§6). For each  $\sigma$  under various  $\theta$ , we execute 20K frames and record the 99.9th percentile latency. Due to space limit, Fig. 4 reports representative power–latency trade-offs with varying  $(M, B)$  and  $\rho_t \in \{25\%, 100\%\}$  under  $MCS = 17$ . Similar trends are observed when varying other cell configuration parameters such as  $\rho_f$  or  $\chi$ . From these measurements, we derive five key observations that guide the design of Nexus.

**Observation 1: The mapping from cell configuration  $\sigma$  to feasibility is highly non-linear.** Our measurements show that whether a cell meets the 3-slot deadline cannot be explained by a single feature. Instead, feasibility depends on complex cross-terms—e.g., a  $2 \times 2$  100 MHz cell with  $\rho_t = 100\%$  may exceed the deadline under a given allocation, while a  $4 \times 4$  100 MHz cell at lower load may remain feasible. This non-straightforward mapping motivates the need for systematic profiling and learning-based models.

**Observation 2: A low-complexity cell can be fully handled in software by a single CPU core without requiring accelerator offloading, e.g.,  $\theta(1, 0|1, 0)$ .** Under light traffic, the baseband workload processed by a single worker core can meet the deadline without offloading LDPC decoding to the accelerator. For example, a single CPU core can support a  $1 \times 1$  400 MHz cell with  $\rho_t = 25\%$  (Fig. 4a).

**Observation 3: A low-complexity cell requiring additional decoding capacity can benefit from adding a single VF alongside one DSP core, e.g.,  $\theta(1, 1|1, 1)$ .** Evaluating and building on the prior work Savannah [27],  $\theta(1, 1|1, 1)$  can sustain a full traffic load ( $\rho_t = 100\%$ ) for a  $1 \times 1$  100 MHz,  $1 \times 1$  200 MHz, or  $2 \times 2$  100 MHz cell. However, this resource allocation is inadequate with increased cell complexity. For instance, the same allocation can only sustain a traffic load of

$\rho_t = 50\%$  for a  $1 \times 1$  400 MHz cell,  $\rho_t = 44\%$  for  $2 \times 2$  200 MHz, and  $\rho_t = 38\%$  for  $4 \times 4$  100 MHz. The bottleneck arises from software DSP stages saturating the single CPU core and from the rising number of MIMO streams feeding the decoder.

**Observation 4: A moderate-complexity cell can be supported by multiple DSP cores and one VF, e.g.,  $\theta(c - 1, 1|c, 1)$  or  $\theta(c, 1|c, 1)$ .** Supporting moderate-complexity cells requires allocating  $c > 1$  CPU cores to software DSP while reserving a single VF for LDPC decoding. Our profiling reveals that the effectiveness of  $\theta(c - 1, 1|c, 1)$  versus  $\theta(c, 1|c, 1)$  depends on the number of available cores. When  $C$  is small (e.g., two or three), the bottleneck lies in software DSP. In such cases, using all cores for DSP, as in  $\theta(2, 1|2, 1)$  for a  $2 \times 2$  200 MHz cell, outperforms  $\theta(1, 1|2, 1)$  and meets the deadline without requiring the extra core that  $\theta(2, 1|3, 1)$  would consume. However, as  $C$  increases, DSP no longer becomes the limiting factor. Here, isolating one core dedicated to ACC100 offloading, i.e.,  $\theta(c - 1, 1|c, 1)$ , effectively eliminates queuing delays at the decoder for a more stable system.

**Observation 5: A high-complexity cell (e.g., larger  $M$ , wider  $B$ , higher  $\chi$ ) requires full offloading across multiple cores and VFs, e.g.,  $\theta(c, c|c, c)$ .** For high-complexity cells (e.g.,  $4 \times 4$  100 MHz), increasing the number of DSP cores alone cannot close the latency gap because a single VF becomes the bottleneck: each additional MIMO stream produces proportionally more code blocks, saturating the decoder. While decoding a  $1 \times 1$  100 MHz cell consumes only about 0.38 Gbps ( $\approx 5\%$  of ACC100’s peak throughput), a  $4 \times 4$  cell scales this demand beyond a single VF’s capacity. To address this, we partition the ACC100 into multiple VFs, distributing decoding tasks in parallel. Balanced configurations in the form of  $\theta(c, c|c, c), \forall c = 1, \dots, \min\{C, V\}$  ensure that each DSP core is “paired” with its own VF, avoiding queuing imbalance. Across diverse cells, this balanced resource allocation strategy achieves the highest throughput, while for low-complexity cells,  $\theta(c - 1, 1|c, 1)$  may still remain preferable due to reduced VF usage and thus power consumption.

**Reduced resource allocation space for a single cell.** The above observations, validated through extensive experiments, allow us to constrain the search to a small but representative subset. In addition, a clear flattening effect can be observed from Fig. 4: as more CPU cores are added, the processing latency eventually stops improving. Beyond this point, allocating additional cores yields diminishing returns. Guided by these observations, we define the reduced feasible resource allocation space for a single cell as:

$$\Theta'(C, V) = \left\{ \begin{array}{ll} \theta(c, 0|c, 0), & c \in \{1, 2, \dots, 6\}, \\ \theta(c, 1|c, 1), & c \in \{1, 2, 3\}, \\ \theta(c - 1, 1|c, 1), & c \in \{4, 5, 6\}, \\ \theta(c, c|c, c), & c \in \{3, 4, 5\}. \end{array} \right. \quad (6)$$

Unlike the full allocation space  $\Theta(C, V)$  in (3), which grows combinatorially, the reduced set has a fixed cardinality of  $|\Theta'(C, V)| = 15$  independent of  $C$  and  $V$  as long as  $\min\{C, V\} \geq 6$ , which is common for a many-core server equipped with a single ACC100 accelerator. For example, with  $C = 32$  and  $V = 16$ , the reduced set still contains only 15 configurations, compared to 152 in the original space.

#### 4.4 Nexus’s Single-Cell Scheduler

While the power model in (5) quantifies the cost of a given resource allocation, it does not establish whether that allocation can meet the 3-slot deadline. Simple rule-based pruning is insufficient: while it captures broad regimes it cannot accurately characterize intermediate cases where feasibility hinges on subtle cross-terms and CPU-ACC100 coupling effects. This motivates the need for a supervised learning model that can generalize from profiling data and reliably map  $(\sigma, \theta)$  to feasibility.

To overcome this challenge, Nexus augments profiling with a supervised learning model that generalizes feasibility from sampled data. Specifically, we train a random forest (RAF) classifier that, for each  $(\sigma, \theta)$  pair, outputs a confidence score  $f(\sigma, \theta) \in [0, 1]$ , representing the probability that the allocation  $\theta$  can meet the 3-slot deadline under configuration  $\sigma$  (see §7 for details). We then define feasibility relative to a decision threshold  $\tau$  (e.g.,  $\tau = 0.5$ ): if  $f(\sigma, \theta) \geq \tau$ , the allocation is labeled *feasible*; otherwise it is *infeasible*. At runtime, given a new and potentially unseen  $\sigma$ , Nexus’s single-cell scheduler evaluates each candidate  $\theta$  from the reduced search space and selects the feasible subset:

$$\mathcal{F}_{\text{RAF}}(\sigma) = \left\{ \theta \in \Theta'(C, V) \mid f(\sigma, \theta) \geq \tau \right\}. \quad (7)$$

Replacing the full allocation space with the reduced search set given by (6), Nexus’s RFA-based single-cell scheduler is:

Optimizing single-cell resource allocation (Opt-1-Cell)
$\theta^* := \arg \min_{\theta \in \Theta'(C, V)} P(\theta) = 7 \cdot C + 1.2 \cdot V$
$\text{s.t. } f(\sigma, \theta) \geq \tau.$

Solving (Opt-1-Cell) returns the most energy-efficient resource allocation  $\theta^*$ , i.e., the number of CPU cores and ACC100 VFs that the cell should use while still meeting the deadline. For example, Fig. 4d shows that while multiple allocations are feasible, (Opt-1-Cell) selects  $\theta(3, 1|3, 1)$  for a  $1 \times 1$  400 MHz cell, achieving the lowest power of 22.2 W. At runtime, the scheduler instantiates this decision by assigning the corresponding physical worker cores and VFs to the cell’s processing pipeline (see §6 for details).

**Model selection rationale.** We select RAF as the feasibility predictor for two reasons. (i) *Capturing non-linear interactions*: feasibility boundaries depend on cross-terms such as

$\rho_t, B, M$ , etc. More importantly, interactions between CPU and ACC100 offloading introduce additional variability (e.g., bbdev queueing, PCIe transfer) that are extremely difficult to model analytically. (ii) *Data efficiency and speed*: compared with DL models, RAF achieves competitive accuracy with substantially less training data and provides real-time  $\mu$ -level inference per  $(\sigma, \theta)$ . As shown in §7, our evaluation against six baselines, demonstrates that RAF delivers the best balance of accuracy, inference latency, and model size.

## 5 Nexus for Multiple Cells

Based on the single-cell resource allocation analysis, we now extend Nexus to support concurrent multi-cell baseband processing with scalability. Nexus, as illustrated in Fig. 1, achieves this through two key components: (i) the parallel instantiation of multiple single-cell processing pipelines, and (ii) a power-aware scheduler that allocates heterogeneous compute resources while considering resource contention.

### 5.1 Multi-cell Resource Allocation Model

While the formulation  $\theta(C^{\text{dsp}}, C^{\text{acc}}|C, V)$  in §4 focuses on single-cell configuration, Nexus is designed to support multi-cell deployments. Consider the scenario where  $N$  cells need to be served by a pool of worker cores and ACC100 VFs. The  $i$ -th cell ( $i = 1, 2, \dots, N$ ) with cell configuration  $\sigma_i$ , may adopt a different resource allocation strategy, denoted by  $\theta_i(C_i^{\text{dsp}}, C_i^{\text{acc}}|C_i, V_i)$ . In this context, we assume that all compute resources, worker cores, and VFs, are assigned in a non-overlapping manner across the cells, i.e.,

$$C_i \cap C_j = \emptyset \text{ and } \mathcal{V}_i \cap \mathcal{V}_j = \emptyset, \forall 1 \leq i \neq j \leq N. \quad (8)$$

This assumption on non-overlapping resource allocation is both practical and widely adopted. Academic platforms (e.g., Agora [11], Hydra [19]) and industry-grade implementations (e.g., srsRAN [37], OAI [24], Intel FlexRAN [21]) all dedicate physical cores to baseband tasks by isolating cores, disabling hyper-threading, and using real-time priorities. Sharing cores across cells introduces non-deterministic context-switching delays: for example, on modern Intel Xeon CPUs, a single round of context switches among four cells can incur  $\approx 60\mu\text{s}$ , which is already 20% of the 3-slot deadline.

To enable concurrent allocations, Nexus adopts a modular architecture with multiple processing pipelines, each bound to a resource allocation  $\theta_i \in \Theta'(C_i, V_i)$  for cell  $i$ . Pipelines are statically compiled but dynamically selected at runtime. At execution, the scheduler determines the appropriate  $\theta_i$  for each active cell and injects the corresponding resource allocation strategy as a configuration entry, activating the desired data path without recompilation. The modularity allows Nexus to support heterogeneous multi-cell deployments with scalability and extensibility: Nexus can easily

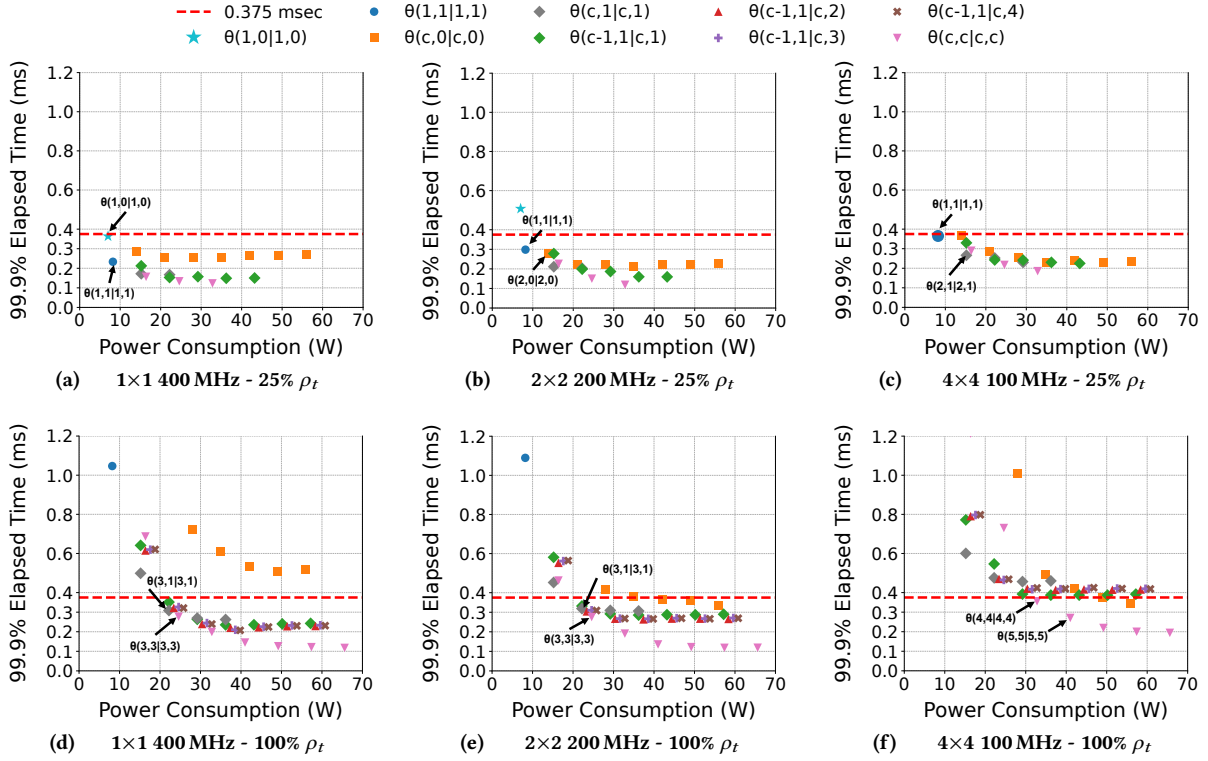


**Figure 4: Power-latency trade-off space for Nexus across heterogeneous cell configurations. Each point represents a distinct resource allocation. Labeled dots indicate the most and second most energy-efficient options that Nexus is likely to select.**

incorporate future accelerators (e.g., GPUs) or hybrid processing models to further maximize resource utilization and system performance.

## 5.2 Nexus Multi-Cell Scheduler

Given a pool of  $C_{\max}$  worker cores and  $V_{\max}$  ACC100 VFs that can be shared to concurrently serve  $N$  cells, Nexus aims to minimize the overall power consumption when allocating compute resources to individual cells,  $N$  cells to achieve minimized energy, i.e.,

Optimizing multi-cell resource allocation (Opt- $N$ -Cell)

$$\{\theta_i^*\}_{i=1}^N := \arg \min_{\{C_i\}, \{V_i\}} \sum_{i=1}^N (7 \cdot C_i + 1.2 \cdot V_i),$$

s.t.  $f(\sigma_i, \theta_i) \geq \tau, \quad \forall i = 1, \dots, N,$   
 $\theta_i \in \Theta'(C_i, V_i)$  from (6),

$$1 \leq \sum_{i=1}^N C_i \leq C_{\max}, \quad 1 \leq \sum_{i=1}^N V_i \leq V_{\max}. \quad (9)$$

However, (Opt- $N$ -Cell) cannot be easily decomposed into  $N$  independent single-cell resource allocation problems of the form (Opt-1-Cell) for two key reasons. First, the latency of a given cell allocation is no longer determined solely by

its local configuration; it is also influenced by system-wide contention such as shared memory bandwidth and PCIe utilization when multiple pipelines execute concurrently. Second, in the multi-cell case, these limited resources,  $C_{\max}$  cores and  $V_{\max}$  VFs, must be partitioned among the  $N$  cells under the constraints described in (9). This yields a combinatorial search space with  $\binom{C_{\max}-1}{N-1} \cdot \binom{V_{\max}-1}{N-1}$  possible partitions. To address these challenges, we develop an energy-aware resource scheduler (Algorithm 1).

**Contention-aware feasibility adjustment via RAF confidence.** Let  $p = f(\sigma_i, \theta_i^{(k)}) \in [0, 1]$  denotes the RAF confidence score, which reflects how likely a configuration  $\theta_i^{(k)}$  in  $\mathcal{F}_{\text{RAF}}(\sigma_i)$  for cell  $i$  satisfies the 3-slot deadline in the single-cell setting. Through controlled experiments, we observed a strong correlation between  $p$  and the empirical latency margin, i.e., the distance between the measured 99.9-th percentile latency and the 3-slot boundary. Hence, we use  $p$  as a proxy for how close the system is to violating the deadline: high  $p$  indicates substantial margin, while low  $p$  indicates the latency is near the boundary.

**Contention-aware latency adjustment via learned linear model.** To capture the impact of running multiple cells concurrently, we introduce a lightweight linear adjustment model that degrades the effective RAF confidence as the

number of active cells  $N$  increases. Specifically, for cell  $i$  and allocation  $\theta_i^{(k)}$ , we define the adjusted confidence as

$$\hat{p}_i^{(k)}(N) = p_i^{(k)} - (\beta_0 + \beta_1 \cdot (N - 1)), \quad (10)$$

where  $p_i^{(k)}$  is the RAF confidence in the single-cell case, and  $(\beta_0, \beta_1)$  are fitted from multi-cell experiments measuring how confidence scores shift as additional cells are activated (example seen in Fig. 6a). A configuration  $\theta_i^{(k)}$  is then considered feasible under  $N$  cells if  $\hat{p}_i^{(k)}(N)$  remains above a threshold  $\tau$ . This approach allows our system to combine Nexus single-cell scheduling with a contention-aware adjustment that generalizes to multi-cell deployments.

**Greedy initialization guided by RAF feasibility (single-cell oracle).** For each active cell  $i$  with features  $\sigma_i$ , we first enumerate the reduced candidate set  $\Theta'(C_i, V_i)$  (15 possible allocations), among which we retain only the RAF-feasible subset

$$\mathcal{F}_{\text{RAF}}(\sigma_i) = \{\theta^{(k)} \in \Theta'(C_i, V_i) \mid f(\sigma_i, \theta^{(k)}) \geq \tau\}, \quad (11)$$

where  $f(\sigma_i, \theta^{(k)}) = 1$  indicates that the RAF classifier predicts the 99.9-th percentile latency under  $(\sigma_i, \theta^{(k)})$  meets the 3-slot deadline in the single-cell setting.

We then order this feasible set by increasing power consumption to form

$$\mathcal{P}_{\text{RAF}}(\sigma_i) = \left\{ \theta^{(1)}, \dots, \theta^{(K)} \mid \theta^{(k)} \in \mathcal{F}_{\text{RAF}}(\sigma_i), \right. \\ \left. P(\theta^{(1)}) < \dots < P(\theta^{(K)}) \right\}. \quad (12)$$

At runtime, we select the first  $\theta^{(k)} \in \mathcal{P}_{\text{RAF}}(\sigma_i)$  whose contention-adjusted feasibility  $\hat{p}_i^{(k)}(N)$  from (10) satisfies  $\hat{p}_i^{(k)}(N) \geq \tau$ , indicating the 99.9-th percentile latency is predicted to meet the 3-slot deadline under  $N$ -cell contention.

**Reduced resource allocation space for  $N$  cells.** To support  $N$  cells on a system equipped with  $C_{\text{max}}$  CPU cores and  $V_{\text{max}}$  ACC100 VFs, a brute-force approach would require evaluating all possible resource allocation combinations across cells. The total number of such allocations is given by:

$$|\{\theta_i\}_{i=1}^N| = \binom{C_{\text{max}} - 1}{N - 1} \cdot \binom{V_{\text{max}} - 1}{N - 1} \quad (13)$$

Nexus addresses this challenge by leveraging its resource allocation scheduler, which reduces the per-cell allocation space to a small fixed set of 15 strategies (Eq. 12). As a result, the multi-cell search complexity becomes linear in  $N$ :

$$|\{\theta'_i\}_{i=1}^N| = 15 \times N \Rightarrow \mathcal{O}(N). \quad (14)$$

For instance, in a 12-cell deployment with  $C_{\text{max}} = 56$  and  $V_{\text{max}} = 16$ , the full brute-force space contains  $\approx 5 \times 10^{12}$  combinations, whereas Nexus's scheduler evaluates only 180, yielding orders-of-magnitude reduction.

This reduced search space enables Nexus to adapt allocations in real time using Algorithm 1. For example, consider

---

### Algorithm 1 Nexus's multi-cell Scheduler

---

**Require:**  $N$  cells with features  $\{\sigma_i\}_{i=1}^N$ ; RAF classifier  $f(\cdot)$  returning feasibility confidence  $[0, 1]$ ; learned contention coefficients  $(\beta_0, \beta_1)$ ; decision threshold  $\tau$ .

**Ensure:** Total compute resource  $(C_{\text{max}}, V_{\text{max}})$  is sufficient to support all  $N$  cells to meet the 3-slot processing deadlines;  $|\mathcal{P}_{\text{RAF}}(\sigma_i)| \geq 1$  for every active cell  $i$ .

```

1: for  $i = 1, 2, \dots, N$  do
2:    $\mathcal{F}_{\text{RAF}}(\sigma_i) \leftarrow \left\{ \theta_i^{(k)} \in \Theta'(C_i, V_i) \mid f(\sigma_i, \theta_i^{(k)}) \geq \tau \right\}$ 
3:    $\mathcal{P}_{\text{RAF}}(\sigma_i) \leftarrow \text{sort } \mathcal{F}_{\text{RAF}}(\sigma_i) \text{ by } P(\cdot)$   $\triangleright$  increasing power
4:   for  $\theta_i^{(k)} \in \mathcal{P}_{\text{RAF}}(\sigma_i)$  do
5:     obtain feasibility confidence  $p_i^k \leftarrow f(\sigma_i, \theta_i^{(k)})$ 
6:      $\hat{p}_i^k \leftarrow p_i^k - (\beta_0 + \beta_1 \cdot (N - 1))$ 
7:     if  $\hat{p}_i^k \geq \tau$  then
8:        $\theta_i(C_i^{\text{dsp}}, C_i^{\text{acc}} | C_i, V_i) \leftarrow \theta_i^{(k)}$ 
9:       break
10:    end if
11:  end for
12: end for
13: Return  $\left\{ \theta_i(C_i^{\text{dsp}}, C_i^{\text{acc}} | C_i, V_i) \right\}_{i=1}^N$ 

```

---

the 2x2 100 MHz cell in Fig. 6. In the single-cell case, Nexus selects  $\theta_i(1, 1|1, 1)$  with a RAF confidence of  $p = 0.542$  as the most energy-efficient configuration meeting the 3-slot deadline. As the number of active cells grows ( $N \geq 4$ ), contention degrades performance and the confidence score drops below the threshold ( $p = 0.469$ ), prompting the scheduler to escalate to  $\theta_i(3, 1|3, 1)$ , the next entry in  $\mathcal{P}_{\text{RAF}}(\sigma_i)$ , thereby restoring deadline compliance. A similar behavior is observed for 4x4 100 MHz cells in Fig. 4f. While  $\theta_i(4, 4|4, 4)$  is sufficient for a single cell, multi-cell contention necessitates escalation to  $\theta_i(5, 5|5, 5)$  to maintain real-time guarantees. Its effectiveness is further demonstrated in the evaluation (Sec.7, Fig.8).

## 6 Implementation

**Multi-cell implementation.** We implement Nexus in about 5,000 lines of C++ code, built on top of the open-source Savannah codebase [27]. Key components include a heterogeneous compute resource scheduler and a set of statically compiled processing pipelines corresponding to different resource allocation strategies. At runtime, Nexus reads the active cell configurations and selects the appropriate pre-compiled resource allocation strategy without requiring recompilation or binary modification.

**Nexus scheduler.** We implement Nexus scheduler in about 300 lines of Python code, including feature extraction, model fitting, and evaluation. The model is trained offline using profiling data (detailed in §7.2), and at runtime Nexus invokes the scheduler during system initialization to minimize overhead. Specifically, the main C++ program calls the Python

scheduler as a subprocess, interpreting each cell’s feature vector  $\sigma$  via JSON input. The scheduler evaluates  $\sigma$  with a set of  $\theta$  and outputs the required resource allocation  $\theta_i^*$  for each active cell—i.e., the number of CPU cores and ACC100 VFs needed to satisfy the 3-slot deadline. These allocations are returned in JSON format and immediately consumed by the C++ runtime, which binds the specified cores and VFs to each cell’s processing pipeline. Because the scheduler runs only at initialization, all subsequent per-slot scheduling decisions are handled natively in C++, ensuring ultra-low Python overhead during real-time operation.

Nexus also includes over 9K example configuration files that cover a wide range of cell configurations and resource allocation strategies, which are used to generate the profiling datasets for model training and testing. To support system-specific adaptation, an automated batch script is also provided to perform single-cell profiling across different cell configurations, enabling users to generate training data that matches their hardware environment.

**ACC100 virtual function (VF) initialization.** We integrate two Silicom Lisbon P2 ACC100 accelerators [34] with Nexus, binding both devices to DPDK’s `igb_uio` driver using the `dpdk-devbind` tool. One ACC100 operates with 16 VFs ( $V_{\max} = 16$ ) while the second is configured in PF mode to enable direct performance comparisons between VF-based and PF-based configurations. To manage VF addressability, we enable the I/O Memory Management Unit (IOMMU) in the system BIOS and kernel. VF configuration parameters, including Queue Groups, DDR memory allocation, and atomic queue settings, are configured through Intel’s `bbdev_pf_bb_config` tool through customized configuration files. To support  $\theta_i(c - 1, 1|c, v)$  and  $\theta_i(c, c|c, c)$ , Nexus utilize DPDK’s threading model and the parallelism of ACC100. We adopt `rte_thread` to create RTE threads with proper CPU affinity, resource isolation, and memory-zone consistency under a single EAL environment. This implementation enables each VF to be attached to a worker core without launching independent EAL instances, supporting up to 16 concurrent VFs per ACC100 hardware accelerator.

**Server configuration.** We perform all profiling (e.g., Fig. 4) and experiments using two Dell PowerEdge R750 servers, interconnected via a Dell EMC PowerSwitch Z29264F-ON using 100 G QSFP28 DAC cables. *Server 1 (srv1) emulates the RUs*, each generating baseband traffic corresponding to multiple UEs. It features a 64-core Intel Xeon Gold 6548N CPU @2.6 GHz with Ubuntu 20.04.2 LTS and an NVIDIA Mellanox ConnectX-6 Dx dual-port 100 GbE SmartNIC. The traffic streams are aggregated and streamed Server 2. *Server 2 (srv2) emulates the DUs*, executing the vRAN baseband processing pipeline with Nexus. It is equipped with a 56-core Intel Xeon Gold 6348 CPU @2.6 GHz running Ubuntu

**Table 2: Random forest performance as a function of forest size. Inference time reported as  $\mu s/(\sigma, \theta)$  at batch size 1.**

# of Trees	Accuracy	Inference Time	Model Size
10	98.99%	1.42 $\mu s$	0.5 MB
50	99.10%	4.45 $\mu s$	2.3 MB
100	99.09%	4.24 $\mu s$	4.4 MB
500	99.08%	21.30 $\mu s$	22.2 MB
1000	99.09%	43.67 $\mu s$	44.4 MB

20.04.6 LTS and an NVIDIA Mellanox ConnectX-5 dual-port 100 GbE NIC. To ensure real-time PHY processing, specific CPU cores are isolated and dedicated to Nexus, which are also responsible for interfacing with two Silicom Lisbon P2 ACC100 accelerators via DPDK 21.11.2. To minimize context switching and optimize performance, we enable performance mode for the CPU and execute Nexus as a real-time process at the highest scheduling priority on both servers. We also disable hyper-threading and employ thread affinity, mitigating the impact of sharing resources among logical cores. `srv2` also runs Nexus’s scheduling framework and evaluates the DL-based and analytical baseline schedulers.

## 7 Evaluation

### 7.1 Experimental Setup

We deploy Nexus with the emulated RUs and DUs instances on separate servers to evaluate the performance. *Server-1* emulates the RUs while *Server-2* emulates the DUs. In addition to the worker cores allocated for DSP and ACC100 tasks ( $C^{\text{dsp}}, C^{\text{acc}}$ ), extra CPU cores are reserved for TX/RX streaming and master control on both the RU and DU sides. Due to the logging overhead, especially when processing large numbers of cells, the system generates substantial log data; for example, recording 100K frames across sixteen cells produces over 2.0 GB of log files. This makes it infeasible to sustain detailed logging beyond sixteen cells without impacting system performance. *However, when logging is disabled, Nexus can support more cells without experiencing processing deferrals, demonstrating its scalability.* We evaluate various cell configuration  $\sigma(M, B, \rho_t, \rho_f, \chi)$ . A processing latency deadline of 3-slot (0.375 ms) is enforced at the 99.9th percentile across all evaluations. We report results along two dimensions: (i) Nexus single-cell scheduler’s performance, and (ii) system-level multi-cell performance.

### 7.2 Single-Cell Scheduler Performance

We first evaluate the feasibility predictors used in Nexus, comparing the proposed Nexus single-cell scheduler with six baselines, including DL and analytical models. Our evaluation focuses on three metrics: (i) accuracy, which refers to the fraction of test samples for which the model correctly predicts feasibility, i.e., whether the 99.9th percentile latency

**Table 3: Deep learning model performance on CPU and GPU. Inference time reported as  $\mu\text{s}/(\sigma, \theta)$  at batch size 1.**

Model	Accuracy	Inference Time (CPU/GPU)	Model Size
MLP	99.14%	582/743 $\mu\text{s}$	55.1 KB
1D CNN	99.26%	615/826 $\mu\text{s}$	52.9 KB
TinyNet	99.34%	570/803 $\mu\text{s}$	30.1 KB

under a given  $(\sigma, \theta)$  defined in §4.3 meets the 3-slot deadline. (ii) inference time per  $(\sigma, \theta)$ , and (iii) model size.

**Datasets.** We collect more than 9K profiling experiments across diverse cell configurations  $\sigma(M, B, \rho_t, \rho_f, \chi)$  and resource allocation strategy  $\theta$ , spanning

- MIMO dimension,  $M \in \{1 \times 1(\text{SISO}), 2 \times 2, 4 \times 4\}$ ,
- Channel BW,  $B \in \{100 \text{ MHz}, 200 \text{ MHz}, 400 \text{ MHz}\}$ ,
- Traffic load,  $\rho_t \in \{25\%, 50\%, 75\%, 100\%\}$ ,
- Transmission BW percentage,  $\rho_f \in \{25\%, 50\%, 75\%, 100\%\}$ ,
- MCS,  $\chi \in \{10, 12, 17, 20\}$ .

For each  $(\sigma, \theta)$  pair, we run Nexus for 20K frames and log detailed timing information of all DSP stages. This *raw logging* produces more than 300 GB of trace data. From these traces, we extract the 99.9th percentile end-to-end processing latency. Each  $(\sigma, \theta)$  is labeled as *feasible* ( $=1$ ) if the latency satisfies the 3-slot deadline, and *infeasible* ( $=0$ ) otherwise, yielding the initial labeled dataset of 9K samples  $(\sigma, \theta)$ .

To broaden coverage, we further augment the dataset using monotonicity rules observed during profiling: (i) if a solution is feasible for  $\rho_t=a$ , then it is also feasible for all  $\rho_t < a$ ; (ii) if infeasible for  $\rho_t=a$ , then it remains infeasible for all  $\rho_t \geq a$ ; (iii) the same monotonicity rule applies to  $\rho_f$ ; (iv) if feasible with  $c$  CPU cores, then it is also feasible for any  $c' > c$ . Similar rules also stand for  $\rho_f$ . Applying these rules expands the dataset to 120,596 labeled samples  $(\sigma, \theta)$ . We split the dataset into train/validation/test sets in a 60/20/20 ratio and use the same splits for RAF, DL models, and mathematical baselines to ensure fair comparison.

**Selecting the forest size.** Table 2 reports the performance of the proposed Nexus single-cell scheduler under different forest sizes. It can be seen that prediction accuracy only marginally improves with larger forests—from 98.99% with 10 trees to 99.10% with 50 trees—after which it quickly saturates. Both the inference time and model size grow linearly with the number of trees. In practice, forests with 50–100 trees provide a favorable tradeoff between accuracy ( $\approx 99.10\%$ ) and efficiency ( $\leq 5 \mu\text{s}$  per inference), and therefore, we empirically select Nexus single-cell scheduler with 50 trees for the remainder of our evaluations.

**Comparison with DL models.** Table 3 compares Nexus single-cell scheduler against three DL models: an MLP [25, 35] with three fully connected layers (128–64–32 neurons

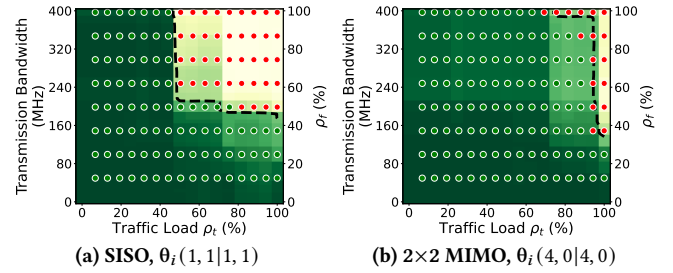


**Figure 5: Nexus single-cell scheduler’s predictions with  $MCS = 18$ . Confidence heatmaps are thresholded at  $\tau = 0.5$  (black dashed line). Each green/red dot corresponds to measured 99.9th processing latency outcomes from executing Nexus over 20K frames.**

with ReLU activations), a 1D CNN [9] with two convolutional layers (32 and 64 filters, kernel size 3) followed by a dense layer (128 neurons), and a TinyNet [17, 44] variant with two depthwise-separable convolutional layers (16 and 32 filters) followed by global average pooling and a dense layer. The three DL models are trained with the same training/validation dataset and evaluated on the same test dataset as Nexus single-cell scheduler to ensure a fair comparison, and they are evaluated on both CPU and GPU. All DL models achieve comparable accuracy ( $\approx 99.20\%$ ), but their inference latency is two orders of magnitude higher than RAF. While GPU execution improves throughput, it introduces non-negligible CPU–GPU transfer overhead, which is why GPU inference in our experiments is often slower than CPU inference. One trade-off is that Nexus single-cell scheduler consumes more memory than compact DL models, since each tree stores explicit branching nodes and split thresholds rather than compressed weight matrices. For example, a 50-tree RAF occupies about 2.2 MB, compared to  $\leq 1$  MB for the DL models. However, this overhead is negligible in modern servers equipped with hundreds of gigabytes of memory and is easily justified by Nexus single-cell scheduler’s significantly lower inference latency and CPU-only deployment.

We further examine sensitivity to input feature dimensionality. For Nexus single-cell scheduler with 50 trees, increasing the input from 4 to 6 features only increases inference latency from 3.09  $\mu\text{s}$  to 3.16  $\mu\text{s}$  (+2.4%). By contrast, DL inference time grows substantially: for a 1D CNN model, increasing from 4 to 6 features increases latency from 613  $\mu\text{s}$  to 636  $\mu\text{s}$  (+3.8%). While the relative percentage increases appear comparable, the absolute overhead is dramatically different: Nexus single-cell scheduler incurs an additional 0.07  $\mu\text{s}$  per  $(\sigma, \theta)$ , whereas the DL model incurs 23  $\mu\text{s}$ . This highlights that RAF inference is effectively insensitive to feature dimensionality, whereas DL inference grows noticeably as features increase due to deeper/wider layers and heavier matrix multiplications. These results directly validate the rationale for adopting RAF outlined in § 4.4.

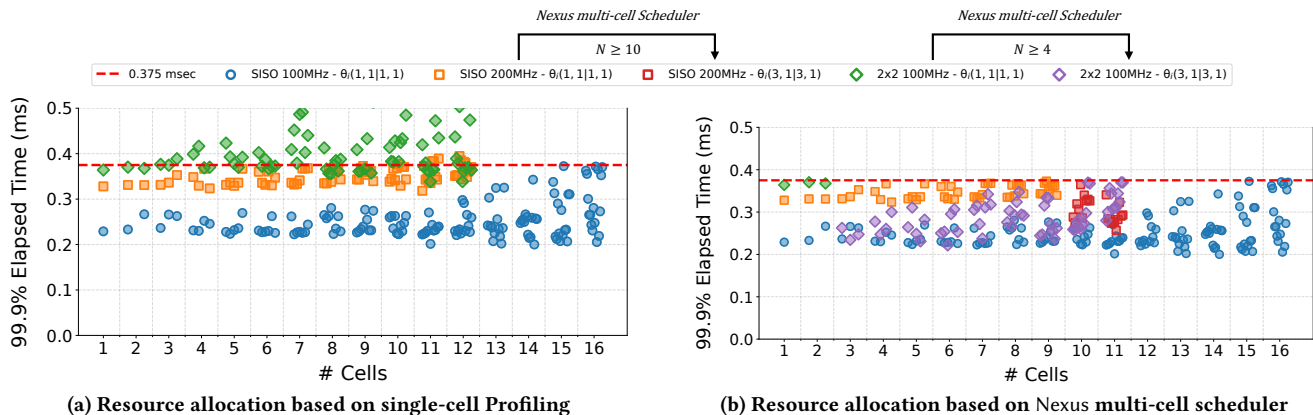


Figure 6: 99.9<sup>th</sup> percentile processing latency vs. the number of concurrently running cells for different cell configurations. Each group of points shows latency measurements for  $N$  cells using the same configuration. In (b), for  $2 \times 2$  100 MHz cells with  $\theta_i(1, 1|1, 1)$ , latency exceeds the deadline when  $N \geq 4$ , prompting Nexus to escalate to  $\theta_i(3, 1|3, 1)$ , restoring compliance.

**Comparison with mathematical baselines.** We also compare the Nexus single-cell scheduler against three lightweight analytical baselines: (i) *logistic regression*, a linear classifier trained on the same features as RAF and DL; (ii) *threshold-based heuristics*, which determine feasibility by applying cutoffs on  $\rho_t$ ,  $B$ , and  $\rho_f$  learned directly from profiling. Specifically, for each feature we identify the maximum feasible value observed in the training set and use these thresholds as decision rules; and (iii) *fixed-zone rules*, which define static feasible regions by combining such thresholds across features and assigning infeasible otherwise. All models are evaluated on the same test set, which ensures that comparisons are consistent and fair. While these analytical baselines are computationally trivial, they perform poorly due to their inability to capture non-linear feature interactions. Logistic regression achieves 93.2% accuracy, and the threshold-based model reaches 92.7%. The fixed-zone rule performs much worse, collapsing to near-random accuracy (42%). These results highlight that such simple models fail to capture the coupling between PHY-layer features, whereas Nexus’s RAF scheduler achieves near-DL accuracy with substantially higher reliability. RAF thus strikes a favorable balance, achieving an accuracy ( $\approx 99.10\%$ ) close to that of the DL models at much faster inference time.

**Generalization to unseen cell configurations.** We next evaluate whether Nexus single-cell scheduler can generalize beyond our dataset by testing on unseen cell configurations. Fig. 5 shows two examples: Fig. 5a represents a SISO cell with MCS18 using  $\theta_i(1, 1|1, 1)$ , and Fig. 5b represents a  $2 \times 2$  MIMO cell with MCS18 using  $\theta_i(4, 0|4, 0)$ , both evaluated under varying  $\rho_t$  and  $\rho_f$ . In these maps, green regions denote configurations predicted to be feasible (meeting the 3-slot deadline), while white regions denote infeasible allocations. The green and red dots correspond to measured ground-truth outcomes from 20K frames (feasible/infeasible,

respectively). It can be seen that Nexus single-cell scheduler achieves strong prediction accuracy of overall 98.8% even for these unseen configurations, with close agreement between predicted feasible regions and measured outcomes. By contrast, traditional models such as threshold-based heuristics fail to capture these non-linear feasibility boundaries, yielding accuracies below 90%. These results confirm that Nexus single-cell scheduler is not only accurate and efficient, but also robust in extrapolating to new cell scenarios.

### 7.3 Multi-Cell Scheduler Performance

All system-level evaluations are conducted at 100%  $\rho_t$ , 100%  $\rho_f$  and  $\chi = 17$  to stress-test Nexus under extreme conditions as MCS17 imposes a higher computational load [11, 27].

**Multi-cell with identical cell configurations and resource allocations.**  $\theta(1, 1|1, 1)$  can reliably meet the 3-slot processing deadline on a single core based on Nexus scheduler for a cell with configurations  $1 \times 1$  100 MHz,  $1 \times 1$  200 MHz, or  $2 \times 2$  100 MHz. We begin by evaluating how many such cells can be simultaneously supported by Nexus under extreme conditions. Fig. 6 shows the results when Nexus simultaneously serves  $N = \{1, 2, \dots, 16\}$  cells with identical configurations, each handled by  $\theta_i(1, 1|1, 1)$ .

Fig. 6 shows that Nexus scales when concurrently serving multiple cells. As illustrated in Fig. 6a, when using  $\theta_i^{(k)}$  directly from the single-cell prediction result, for  $1 \times 1$  100 MHz cells, Nexus supports up to sixteen simultaneous cells using a total number of sixteen worker cores and sixteen ACC100 VFs, resulting in aggregated data rate of 3.91 Gbps. However,  $1 \times 1$  200 MHz and  $2 \times 2$  200 MHz cells present corner cases. As we are running ten  $1 \times 1$  200 MHz cells or four  $2 \times 2$  100 MHz cells, their single-cell confidence rate is already near the threshold under  $\theta(1, 1|1, 1)$ , and additional parallel cells introduce contention that causes deadline violations (see §5.2).

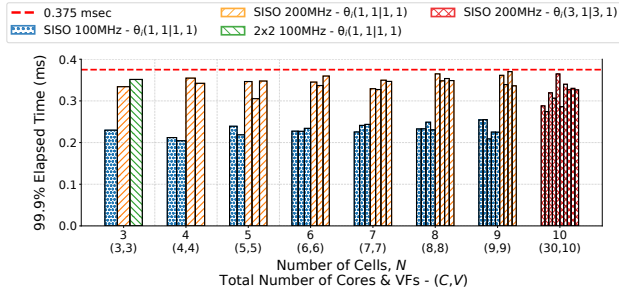


**Figure 7: 99.9<sup>th</sup> percentile processing latency for heterogeneous cell configurations processed concurrently using the same resource allocation.**

In response, Nexus would transition to the next  $\theta_i^{(k)}$  in  $\mathcal{P}_{\text{RAF}}$ , which is  $\theta_i(3, 1|3, 1) \forall i$  for those cells. As shown in Fig. 6b, by adjusting resource allocation to  $\theta_i(3, 1|3, 1)$  for each cell, Nexus supports up to eleven cells for both  $1 \times 1$  200 MHz and  $2 \times 2$  100 MHz while meeting the 3-slot processing deadline, with a total number of 33 worker cores and 11 ACC100 VFs, resulting in an aggregated data rate of 5.37 Gbps. Our experiments are limited to eleven cells, which already occupy 55 of the 56 available cores (including streaming and master cores). It is worth noting that even when the same allocation strategy appears unchanged across different  $N$ , the multi-cell scheduler is still actively evaluating feasibility through RAF confidence. For example, in the case of  $1 \times 1$  100 MHz cells with  $\theta_i(1, 1|1, 1)$ , the RAF confidence decreases from  $p=0.87$  at  $N=1$  to  $p=0.53$  at  $N=16$ . Although contention reduces the margin, the confidence remains above the threshold  $\tau$ , so the allocation is considered feasible for all sixteen cells.

**Multi-cell with heterogeneous cell configurations and identical resource allocations.** Next, we evaluate Nexus’s ability to handle heterogeneous cells while employing identical resource allocations for each cell. Fig. 7 shows the 99.9th-percentile processing latency when Nexus concurrently serves  $N = \{3, 4, 5, 6, 7, 8, 9, 10\}$  cells with  $\theta_i(1, 1|1, 1)$  or  $\theta_i(3, 1|3, 1)$ . The results for  $N$  cells have  $N$  bars, corresponding to the 99.9th-percentile processing latency for each of the  $N$  cells. When running nine cells—five  $1 \times 1$  100 MHz cells and four  $1 \times 1$  200 MHz cells—Nexus processes all frames within the 3-slot deadline, achieving a total data rate of 3.17 Gbps using overall nine worker cores and nine ACC100 VFs, simultaneously supporting heterogeneous cell configurations.

**Multi-cell with heterogeneous cell configurations and heterogeneous resource allocations.** Finally, we evaluate the performance of Nexus in scenarios with heterogeneous cell configurations that use different processing techniques. Fig. 8 shows the 99.9th-percentile processing time for individual cells when Nexus concurrently serves

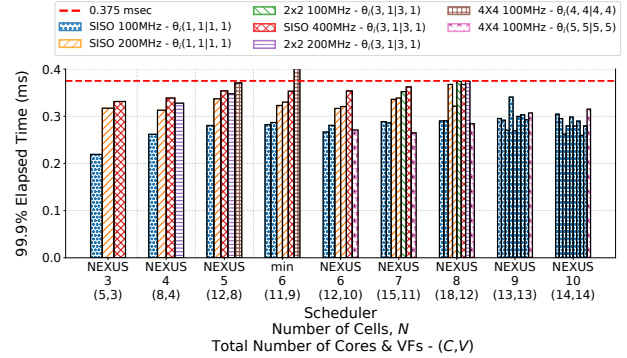


**Figure 8: 99.9<sup>th</sup> percentile processing latency for heterogeneous cells with heterogeneous resource allocation. Nexus represents the scheduler proposed in this work, while *min* represents using resources based on single-cell profiling.**

$N = \{3, 4, 5, 6, 7, 8, 9, 10\}$  heterogeneous cells. When configured to serve five cells with a 5-th  $4 \times 4$  100 MHz cell with high complexity, Nexus selects  $\theta_5(4, 4|4, 4)$  to handle this cell based on Algorithm 1. Fig. 8 shows all five cells with a total data rate of 2.68 Gbps using 12 worker cores and eight ACC100 VFs are able to meet the 3-slot deadline.

For the scenario with six cells, the prediction confidence for a  $4 \times 4$  100 MHz cell processing latency under resource allocation  $\theta_6(4, 4|4, 4)$  was estimated to be infeasible based on (10) and is experimentally confirmed in Fig. 8 using the *min* scheduler across six cells. In response, Nexus invokes its multi-cell scheduler and adjusts the resource allocation for this cell to  $\theta_6(5, 5|5, 5)$ . With this updated resource allocation, the latency is improved to 0.268 ms. As a result, the corresponding bar for the  $4 \times 4$  100 MHz cell appears lower in the six-cell case than in the five-cell case in Fig. 8. This adaptive resource reassignment enables all six cells to meet their real-time processing deadlines, achieving a total data rate of 3.41 Gbps using 12 worker cores and 10 ACC100 VFs. The results highlight Nexus’s ability to scale to highly heterogeneous deployments while maintaining real-time guarantees.

## 8 Conclusion

In this paper, we presented Nexus, the first system to enable efficient virtualized, multi-cell mmWave PHY baseband processing on a single heterogeneous compute server. Nexus addresses the growing need for efficient computational resource sharing in vRAN systems. We introduced detailed mechanisms for sharing the Intel ACC100 accelerator across multiple cores and Virtual Functions, supported by a RAF-based scheduler that minimizes power consumption while meeting real-time deadlines. Our evaluation demonstrates that Nexus supports up to sixteen concurrent cells with a combined data rate of 5.37 Gbps and more when logging is disabled across diverse deployment scenarios. By bridging

the gap between baseband computation and resource virtualization, Nexus opens the door to scalable and energy-efficient vRAN architectures.

## Acknowledgments

This work was supported in part by NSF grants CNS-2211944, AST-2232458, CNS-2330333, and CNS-2443137. This work was also supported in part by the Center for Ubiquitous Connectivity (CUBiC), sponsored by Semiconductor Research Corporation (SRC) and Defense Advanced Research Projects Agency (DARPA) under the JUMP 2.0 program. We thank Anuj Kalia (Microsoft), Rahman Doost-Mohammady and Andrew Sedlmayr (Rice University), and Danyang Zhuo (Duke University) for their contributions to this work.

## References

- [1] 2024. Intel Performance Counter Monitor. <https://github.com/intel/pcm>.
- [2] 2025. NEXUS: Efficient and scalable multi-cell mmWave baseband processing with heterogeneous compute. <https://github.com/functions-lab/agora-mmwave>.
- [3] 3GPP. 2017. *Study on new radio access technology: Radio access architecture and interfaces*. Technical Specification (TS) 38.801. 3rd Generation Partnership Project (3GPP). Version 14.0.0.
- [4] 3GPP. 2018. *5G; NR; Physical Layer Procedures for Data*. Technical Specification (TS) 38.214. 3rd Generation Partnership Project (3GPP). [https://www.etsi.org/deliver/etsi\\_ts/138200\\_138299/138214/15.02.00\\_60/ts\\_138214v150200p.pdf](https://www.etsi.org/deliver/etsi_ts/138200_138299/138214/15.02.00_60/ts_138214v150200p.pdf) Version 15.2.0.
- [5] 3GPP. 2019. *5G; NR; Physical Layer Procedures for Control*. Technical Specification (TS) 38.213. 3rd Generation Partnership Project (3GPP). [https://www.etsi.org/deliver/etsi\\_ts/138200\\_138299/138213/15.06.00\\_60/ts\\_138213v150600p.pdf](https://www.etsi.org/deliver/etsi_ts/138200_138299/138213/15.06.00_60/ts_138213v150600p.pdf) Version 15.6.0.
- [6] 3GPP. 2022. *5G; NR; User Equipment (UE) radio transmission and reception; Part 1: Range 1 Standalone*. Technical Specification (TS) 38.101-1. 3rd Generation Partnership Project (3GPP). [https://www.etsi.org/deliver/etsi\\_ts/138100\\_138199/138101/17.05.00\\_60/ts\\_138101v170500p.pdf](https://www.etsi.org/deliver/etsi_ts/138100_138199/138101/17.05.00_60/ts_138101v170500p.pdf) Version 17.5.0.
- [7] 3GPP. 2022. *5G; NR; User Equipment (UE) radio transmission and reception; Part 2: Range 2 Standalone*. Technical Specification (TS) 38.101-2. 3rd Generation Partnership Project (3GPP). [https://www.etsi.org/deliver/etsi\\_ts/138100\\_138199/138102/17.06.00\\_60/ts\\_138102v170600p.pdf](https://www.etsi.org/deliver/etsi_ts/138100_138199/138102/17.06.00_60/ts_138102v170600p.pdf) Version 17.6.0.
- [8] Qing An, Santiago Segarra, Chris Dick, Ashutosh Sabharwal, and Rahman Doost-Mohammady. 2023. A deep reinforcement learning-based resource scheduler for massive MIMO networks. *IEEE Trans. Mach. Learn. Commun. Netw.* 1 (2023), 242–257.
- [9] Meliboev Azizjon, Alikhanov Jumabek, and Wooseong Kim. 2020. 1D CNN based network intrusion detection with normalization on imbalanced data. In *Proc. IEEE ICAIC'20*.
- [10] I Chih-Lin, Jinri Huang, Ran Duan, Chunfeng Cui, Jesse Jiang, and Lei Li. 2014. Recent progress on C-RAN centralization and cloudification. *IEEE Access* 2 (2014), 1030–1039.
- [11] Jian Ding, Rahman Doost-Mohammady, Anuj Kalia, and Lin Zhong. 2020. Agora: Real-time massive MIMO baseband processing in software. In *Proc. ACM CoNEXT'20*.
- [12] Xiaoran Fan, Zhenzhou Qi, Zhenhua Jia, and Yanyong Zhang. 2018. Enabling concurrent IoT transmissions in distributed C-RAN. In *Proc. ACM SenSys'18*.
- [13] Rostand AK Fezeu, Jason Carpenter, Claudio Fiandrino, Eman Ramadan, Wei Ye, Joerg Widmer, Feng Qian, and Zhi-Li Zhang. 2023. Mid-Band 5G: A measurement study in Europe and US. *arXiv preprint arXiv:2310.11000* (2023).
- [14] Xenofon Foukas and Bozidar Radunovic. 2021. Concordia: Teaching the 5G vRAN to share compute. In *Proc. ACM SIGCOMM'21*.
- [15] Zhihui Gao, Zhenzhou Qi, and Tingjun Chen. 2024. Mambas: Maneuvering analog multi-user beamforming using an array of subarrays in mmWave networks. In *Proc. ACM MobiCom'24*.
- [16] Andres Garcia-Saavedra, Xavier Costa-Perez, Douglas J Leith, and George Iosifidis. 2018. FluidRAN: Optimized vRAN/MEC orchestration. In *Proc. IEEE INFOCOM'18*.
- [17] Giuse. 2023. TinyNet. <https://github.com/giuse/tinynet>.
- [18] Global System for Mobile Communications. 2020. 5G TDD synchronization guidelines and recommendations for the coexistence of TDD networks in the 3.5 GHz range. <https://www.gsma.com/spectrum/wp-content/uploads/2020/04/3.5-GHz-5G-TDD-Synchronisation.pdf>.
- [19] Junzhi Gong, Anuj Kalia, and Minlan Yu. 2023. Scalable distributed massive MIMO baseband processing. In *Proc. USENIX NSDI'23*.
- [20] David Hunt, Kristen Angell, Zhenzhou Qi, Tingjun Chen, and Miroslav Pajic. 2024. MadRadar: A black-box physical layer attack framework on mmWave automotive FMCW radars. In *Proc. ISOC NDSS'24*.
- [21] Intel Corporation. 2019. FlexRAN LTE and 5G NR FEC software development kit modules. <https://www.intel.com/content/www/us/en/developer/articles/technical/flexran-lte-and-5g-nr-fec-software-development-kit-modules.html>.
- [22] Nikita Lazarev, Tao Ji, Anuj Kalia, Daehyeok Kim, Ilias Marinos, Francis Y Yan, Christina Delimitrou, Zhiru Zhang, and Aditya Akella. 2023. Resilient baseband processing in virtualized RANs with SlingShot. In *Proc. ACM SIGCOMM'23*.
- [23] Biraja Mahapatra. 2022. Intel + Radisys FlexRAN success stories. [https://networkbuilders-cdn.s3.us-east-2.amazonaws.com/Intel\\_Radisys\\_FlexRAN\\_Success\\_Stories\\_Biraja\\_Prasad\\_Mahapatra.pdf](https://networkbuilders-cdn.s3.us-east-2.amazonaws.com/Intel_Radisys_FlexRAN_Success_Stories_Biraja_Prasad_Mahapatra.pdf).
- [24] OpenAirInterface. 2023. openairinterface5G. [https://gitlab.eurecom.fr/oai/openairinterface5g/blob/develop/doc/FEATURE\\_SET.md](https://gitlab.eurecom.fr/oai/openairinterface5g/blob/develop/doc/FEATURE_SET.md).
- [25] Marius-Constantin Popescu, Valentina E Balas, Lilianna Perescu-Popescu, and Nikos Mastorakis. 2009. Multilayer perceptron and neural networks. *WSEAS TCS* 8, 7 (2009), 579–588.
- [26] Zhenzhou Qi, Zhihui Gao, Chung-Hsuan Tung, and Tingjun Chen. 2023. Programmable millimeter-wave MIMO radios with real-time baseband processing. In *Proc. ACM WiNTECH'23*.
- [27] Zhenzhou Qi, Chung-Hsuan Tung, Anuj Kalia, and Tingjun Chen. 2024. Savannah: Efficient mmWave Baseband Processing with Minimal and Heterogeneous Resources. In *Proc. ACM MobiCom'24*.
- [28] Sundeep Rangan, Theodore S Rappaport, and Elza Erkip. 2014. Millimeter-wave cellular wireless networks: Potentials and challenges. *Proc. of the IEEE* (2014).
- [29] Theodore S Rappaport, Shu Sun, Rimma Mayzus, Hang Zhao, Yaniv Azar, Kevin Wang, George N Wong, Jocelyn K Schulz, Mathew Samimi, and Felix Gutierrez. 2013. Millimeter wave mobile communications for 5G cellular: It will work! *IEEE Access* 1 (2013), 335–349.
- [30] Dipankar Raychaudhuri, Ivan Seskar, Gil Zussman, Thanasis Korakis, Dan Kilper, Tingjun Chen, Jakub Kolodziejewski, Michael Sherman, Zoran Kostic, Xiaoxiong Gu, et al. 2020. Challenge: COSMOS: A city-scale programmable testbed for experimentation with advanced wireless. In *Proc. ACM MobiCom'20*.
- [31] John W Romein and Bram Veenboer. 2018. Powersensor 2: A fast power measurement tool. In *Proc. IEEE ISPASS'18*.
- [32] Bodhisatwa Sadhu, Yahya Tousei, Joakim Hallin, Stefan Sahl, Scott K Reynolds, Örjan Renström, Kristoffer Sjögren, Olov Haapalahti, Nadav Mazor, Bo Bokinge, et al. 2017. A 28-GHz 32-element TRX phased-array IC with concurrent dual-polarized operation and orthogonal

- phase and gain control for 5G communications. *IEEE J. Solid-State Circuits* 52, 12 (2017), 3373–3391.
- [33] Leonardo Lo Schiavo, Gines Garcia-Aviles, Andres Garcia-Saavedra, Marco Gramaglia, Marco Fiore, Albert Banchs, and Xavier Costa-Perez. 2024. CloudRIC: Open radio access network (O-RAN) virtualization with shared heterogeneous computing. In *Proc. ACM MobiCom'24*.
- [34] Silicom Ltd. 2023. Lisbon P2 ACC100 FEC accelerator extended temp. <https://www.silicom-usa.com/wp-content/uploads/2023/09/Lisbon-P2-ACC100-FEC-Accelerator-Extended-temp-1v1.pdf>.
- [35] Jaswinder Singh and Rajdeep Banerjee. 2019. A study on single and multi-layer perceptron neural network. In *IEEE ICCMC'19*.
- [36] Sameer Kumar Singh, Rohit Singh, and Brijesh Kumbhani. 2020. The evolution of radio access network towards open-RAN: Challenges and opportunities. In *Proc. IEEE WCNCW'20*.
- [37] srsRAN Project. 2023. srsRAN Project Documentation - Features and Roadmap. [https://docs.srsran.com/projects/project/en/latest/general/source/2\\_features\\_and\\_roadmap.html](https://docs.srsran.com/projects/project/en/latest/general/source/2_features_and_roadmap.html).
- [38] Kun Tan, He Liu, Jiansong Zhang, Yongguang Zhang, Ji Fang, and Geoffrey M Voelker. 2011. Sora: high-performance software radio using general-purpose multi-core processors. *Commun. ACM* 54, 1 (2011), 99–107.
- [39] Chengke Wang, Hao Nie, Weiguo Wang, Junchen Guo, Pengyu Zhang, Yulong Chen, Shunmin Zhu, Yuan He, and Chenren Xu. 2024. Understanding 5G Performance on Heterogeneous Computing Architectures. *IEEE Commun. Mag.* (2024).
- [40] Mohamad Saalim Wani, Mathias Kretschmer, Bernd Schröder, Andreas Grebe, and Michael Rademacher. 2024. Open RAN: A concise overview. *IEEE Open J. Commun. Soc.* 6 (2024), 13–28.
- [41] Timothy Woodford, Xinyu Zhang, Eugene Chai, Karthikeyan Sundaresan, and Amir Khojastepour. 2021. Spacebeam: Lidar-driven one-shot mmwave beam management. In *Proc. ACM MobiSys'21*.
- [42] Jun Wu, Zhifeng Zhang, Yu Hong, and Yonggang Wen. 2015. Cloud radio access network (C-RAN): A primer. *IEEE Network* 29, 1 (2015), 35–41.
- [43] Jiarong Xing, Junzhi Gong, Xenofon Foukas, Anuj Kalia, Daehyeok Kim, and Manikanta Kotaru. 2023. Enabling resilience in virtualized RANs with Atlas. In *Proc. ACM MobiCom'23*.
- [44] Kunran Xu, Yishi Li, Huawei Zhang, Rui Lai, and Lin Gu. 2022. EtinyNet: Extremely tiny network for TinyML. In *Proc. AAAI'22*.
- [45] Qing Yang, Xiaoxiao Li, Hongyi Yao, Ji Fang, Kun Tan, Wenjun Hu, Jiansong Zhang, and Yongguang Zhang. 2013. BigStation: Enabling scalable real-time signal processing in large MU-MIMO systems. *ACM SIGCOMM Computer Communication Review* 43, 4 (2013), 399–410.
- [46] Renjie Zhao, Timothy Woodford, Teng Wei, Kun Qian, and Xinyu Zhang. 2020. M-Cube: A millimeter-wave massive MIMO software radio. In *Proc. ACM MobiCom'20*.